Coupled carbon structure and iron species for multiple periodate-based oxidation reaction

Ling Xiang [a,1], Eydhah Almatrafi [b,1], Hailan Yang [a], Haoyang Ye [a], Fanzhi Qin [a], Huan Yi [a], Yukui Fu [a], Xiuqin Huo [a], Wu Xia [a], Hong Li [a], Ming Yan [a], Chengyun Zhou [a,b], Guangming Zeng [a,b*], Xiaofei Tan [a,*]

[a] *College of Environmental Science and Engineering, Hunan University, and Key Laboratory of Environmental Biology and Pollution Control (Hunan University), Ministry of Education, Changsha 410082, P.R. China.*

[b] *Center of Research Excellence in Renewable Energy and Power Systems, Center of Excellence in Desalination Technology, Department of Mechanical Engineering, Faculty of Engineering-Rabigh, King Abdulaziz University, Jeddah 21589, Saudi Arabia.*

* Corresponding authors: Tel.: +86–731–88822754; fax: +86–731–88823701.

Email address: zgming@hnu.edu.cn (Guangming Zeng) and tanxf@hnu.edu.cn (Xiaofei Tan)

[1] These authors contribute equally to this article

Abstract

The vital roles of synergetic carbon structure and iron species in periodate (PI)-based oxidation reaction remains unclear. In this study, multiple active species were identified as Fe(IV), $^1O_2$, $\bullet O_2^-$, and $IO_3\bullet$ in the magnetic ferrite-modified biochar (MFBC)/PI process. The MFBC/PI system maintained stable degradation efficiency under wide pH ranges and the presence of various interfering anions. A unique continuous cycle experiment verifies the contribution of iron leaching-precipitation equilibrium and redox equilibrium to the degradation efficiency of PI/MFBC system. Moreover, except carbonyl functional groups (C=O) on biochar could activate PI, the interacted biochar-Fe provides an active site dispersion and fast electron transfer. The attack sites and degradation pathways on DDA were determined with DFT, P and S atoms on diphenylamine dithiophosphoric acid (DDA) were suggested to be the most active sites in MFBC/PI systems. Overall, this work investigated the mechanism of PI activation by the synergistic metal-carbon at the solid-liquid interface of heterogeneous catalysts, would provide a new perspective into the catalytic activation of PI by iron-carbon composites.

Keywords: Iron-carbon composites; Periodate; Advanced oxidation processes; Synergetic effects; Density functional theory.

Graphical Abstract:

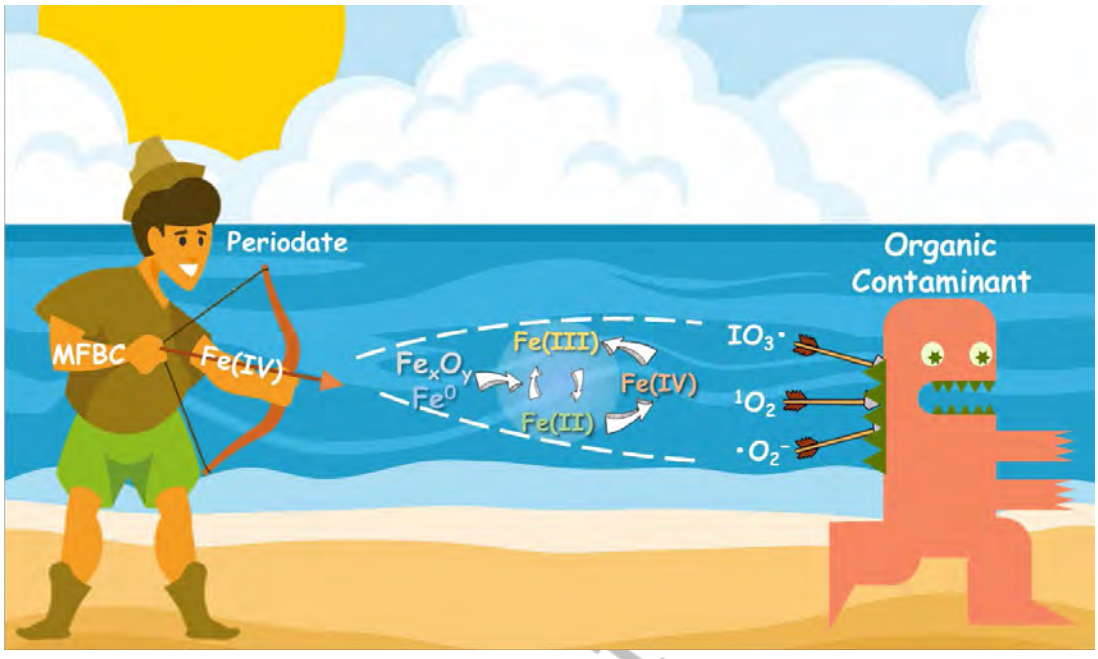

1 Introduction

Advanced oxidation processes (AOPs) have been regarded as important means of treating refractory wastewater [1-3]. The AOPs technologies mainly include Fenton, Fenton-like, sulfate radical advanced oxidation, photocatalysis, etc [4-6]. Recently, periodate (PI, IO_4^-, E_0 = + 1.60 V) has attracted extensive attention because it could produce iodine radicals with strong oxidation capacity, such as IO_3• and IO_4• after activation [1, 2]. Moreover, radical chain reactions also bring about secondary radical active species such as superoxide radicals ($•O_2^-$) or non-radical active species singlet oxygen ($^1O_2$), which jointly participate in the degradation of organic pollutants [7]. In previous studies, PI has been activated by ultraviolet light (UV) or visible light radiation (VL), transition metals, ultrasound, and other means to generate more reactive substances, thereby improving the degradation efficiency of PI-AOPs towards organic pollutants [8-10]. Particularly, transition metal-based activators (such as Fe, Mn and Co) are promising activation choices due to their low cost and excellent activation efficiency [9, 11]. However, transition metal catalysts even like Fe are constrained in their practical application by their potential metal leaching risk and low redox cycling capacity [12]. Therefore, the exploration of novel transition metal-based catalysts is of significance for the application of PI.

Adopting suitable support materials is an important way to improve the performance of iron-based catalysts and reduce the environmental impact [13-15]. Biochar has been widely used as adsorbents, catalysts, or carriers of catalytically active

substances in the field of environmental remediation because of its low cost, diverse structure, economic and environmental friendliness [16, 17]. Because of the porous structure of biochar, Fe and its oxides-loaded biochar could effectively utilize the synergistic activation effects of biochar and transition metals on one hand, and on the other hand, biochar could disperse and stabilize iron oxides to enhance the catalytic performance. Numerous investigations have been focused on the application of biochar catalyst for persulfate AOPs or Fenton [18]. In conclusion, it is a mature strategy to prepare magnetic ferrite-modified biochar (MFBC) catalyst by combining biochar and iron for activating PI. To the best of our knowledge, in the PI/magnetic ferrite-modified biochar (PI/MFBC) system, the vital roles of composited carbon structure and iron species in PI-based oxidation reaction remain unclear.

Flotation is the preferred and most effective method for metal beneficiation [19]. Diphenylamine dithiophosphoric acid (aniline aerofloat, DDA) is a widely used flotation agent containing sulfur (S) and phosphorus (P) sites [20, 21] in reality. A large amounts of wastewater containing DDA could be discharged directly into the environment, thereby causing a negative effect on the soil, aquatic ecosystems, even biochemical treatment system [22, 23]. More importantly, DDA is easy to produce aniline organic matter in the environment, which poses a serious threat to the ecological environment and human healthy [24]. Therefore, it is urgent to propose a water treatment technology that could stably and efficiently remove aniline flotation. Compared with other flotation agents, DDA has better mineral processing performance

and more applications. Based on above reasons, DDA was selected as a model pollutant in this experiment, to explore the degradation treatment of a class of pollutants containing S and P sites by the MFBC/PI system.

In this study, yellow bamboo was selected as biomass to prepare MFBC due to its high carbon content [25]. As for the choice of iron source, ferrate could form alkali for modification of biomass and produce gases for pore formation [26]. Moreover, compared with other commonly used iron salts, such as $Fe(NO_3)_3 \cdot 9H_2O$ (13.9%), $FeCl_3 \cdot 6H_2O$ (20.7%), and $Fe_2(SO_4)_3 \cdot 9H_2O$ (19.9%), ferrate could achieve the less reagent usage but more loaded iron due to its high iron content (28.2%). Thus, ferrate was used to modify yellow bamboo to produce MFBC. By utilizing the MFBC prepared above, the intrinsic mechanism and synergistic effect between carbon structure and iron species in catalytic activation of PI were investigated. Multiple characterizations were conducted to confirm the effect of Fe on carbon structure and possible active sites. Quenching, PMSO oxidation, and electron paramagnetic resonance (EPR) were used to identify active species and the behavioral changes of iron species in the PI/MFBC system. Moreover, a unique continuous cycle experiment was used to further investigate the nature of iron species. Finally, DFT analysis was used to evaluate the degradation performance and attack sites of organic pollutants containing S and P in the PI/MFBC system.

2 Materials and methods

2.1 Chemicals and materials

See Text S1 for chemicals utilized. Magnetic ferrite-modified biochar (MFBC) was prepared by impregnation-pyrolysis method. In general, 2.00 g yellow bamboo was used as biomass source. 1.98 g K_2FeO_4 (equivalent to 0.01 M Fe) were magnetically mixed in 100 mL DI water for 24 h. Then, the mixture was transferred into oven at 105 °C until constant weight. The dried precipitation was ground and transferred to quartz boat for pyrolysis in tubular furnace. The pyrolysis processes are as follows: (a) from room temperature to 100 °C with the heating rate of 6 °C/min, held for 1 h in N_2 flow; (b) continue to increase temperature to 500 °C, 650 °C and 800 °C with the heating rate of 6 °C/min, held for 4 h in N_2 flow, then cool to room temperature without control; (3) the materials named MFBC according to the pyrolysis temperature (MFBC-500 and MFBC-800). The pristine bamboo biochar (BBC) was prepared followed the same steps of MFBC-800 without K_2FeO_4 addition.

2.2 Analytical methods

DDA concentration was determined by Agilent 1100 high performance liquid chromatography (HPLC, USA) with C18 (5 μm, 250 × 4.6 mm) HPLC column. The mobile phase are methanol and water (v: v = 55: 45). The flow velocity was 1 mL/min. The injection volume was 20 μL and the detection wavelength was set to 233 nm. The content of iron in the reaction solution was determined by PinAAcle 900F flame atomic spectrophotometer (AAS, USA). Gas chromatography-mass spectrometry (GC-MS, Shimadzu 2020, Japan) was used to identify intermediates of DDA [27]. The chromatographic column was RTX-5MS (30 m × 0.25 mm × 0.25 μm), the inlet

temperature was 280 °C, the injection volume was 1 μL, the flow rate was 1 mL/min, and the carrier gas was helium. The initial temperature was 40 °C and heated to 100 °C with heating rate of 5 °C/min and hold for 0 min. Then heating rate at 15 °C/min to 280 °C hold for 0 min. Finally, heating rate at 30 °C/min to 330 °C, hold for 0 min.

2.3 Characterization methods

X-ray diffraction pattern (XRD, Rigaku SmartLab SE, Japan) in the range of 10~80° (5°/min) was recorded. Scanning electron microscope (SEM) and energy-dispersive X-ray spectroscopy (EDS) image were investigated by TESCAN MIRA LMS (Czech) and Oxford instruments (UK). X-ray photoelectron spectroscopy (XPS) was tested using Thermo Scientific Escalab 250Xi (USA). Electron spin resonance (ESR) tests were used to identify transient free radicals by Bruker spectrometer (Germany). Fourier-transform infrared spectroscopy (FT-IR) was measured using Thermo Scientific Nicolet iS20 (USA). The surface properties were determined by Quantachrome Autosorb IQ, Austria. Raman spectroscopy was used to determine the defect structure (Edinburgh RM5 / XploRA, UK).

2.4 Catalytic degradation of DDA

The catalytic properties of the materials prepared for degradation of DDA were investigated in 150 mL flask containing 100 mL 5 mg/L DDA (the initial pH was adjusted to 7.0 ± 0.1 using 0.5 M NaOH and 0.5 M HCl). In general, 0.2 g/L catalysts and 0.25 g/L PI were added to DDA solution, and successively shaking at a constant rate of 130 rpm in thermostatic oscillator. 0.9 mL mixture was sampled at 5 min, 15

min, 30 min, 45 min, and 60 min, passed through 0.22 μm sterile syringe filters, and injected into the sample bottle containing 0.1 mL dimethyl sulfoxide (DMSO).

The cycle experiment was used to study the properties of the iron active site in MFBC-800. Take two conical flasks (marked A and B), add 5 mg/L DDA, 0.25 g/L PI, and 0.2 g/L MFBC-800, take 1mL from A at 5 min, 15 min, 30 min, 45 min and 60 min, respectively, for the determination of DDA. Another 1ml was taken out for determination of total free iron. Considering that the degradation of DDA by MFBC/PI system can be up to 90%, after the first degradation, solid DDA and PI were added to B again to restore the concentration to the original level, and the degradation continued. Also, 1 mL was taken from B at 5 min, 15 min, 30 min, 45 min, and 60 min for the determination of DDA, and another 1 mL was taken for the determination of total free iron concentration.

The contributions of MFBC derived-dissolved organic matter (DOM) and unstable bonded iron from the MFBC were also investigated. 0.2 g/L of MFBC-800 was thoroughly mixed with DI water for 24 h, and the supernatant was taken after filtration. Using the supernatant as a solvent, DDA was added to prepare a 5 mg/L DDA solution. 0.25 g/L PI was added for DDA degradation experiments. The effect of adsorption on the final removal of DDA was studied. After PI-AOPs reaction, MFBC was magnetically collected and DDA desorption was performed in ethanol. All experiments were performed at least three times.

2.5 Theoretical calculation

In this study, Gaussian software package (g16) was used to study the degradation of DDA by MFBC/PI system [28, 29]. A wave function analysis software, Multiwfn was used to study the Fukui function of DDA molecule, which was used to predict the attack trend and site in the reaction process [30]. Refer to Text S2 for more information.

2.6 Identification of iodine species

PI-AOPs often produced a series of iodine disinfection by-products, some of which could have potential environmental risks. Therefore, it was necessary to evaluate the toxicity of these byproducts [31]. Detailed determination methods were provided in Text S3 [9].

3 Results and discussion

3.1 Material characterizations

The SEM and the corresponding EDS images of BBC and MFBC are shown in Figures S1 and S2. The sections within the white line highlight the structural differences between the various materials. The BBC was observed with a porous structure and a relatively smooth surface (Figure S1a). After modification, the pore structure of biochar was retained, but the surface of MFBC became rough and uneven. Meanwhile, distinctive spherical particles coated on MFBC could be easily observed (Figures S1b -d). The EDS results shown the presence of iron on surface of MFBCs. 3.0 wt%, 3.9 wt%, and 13.7 wt% iron on the MFBC-500, MFBC-650, and MFBC-800, respectively (Figure S2b-d and Table S1). Overall, combining SEM and EDS images could be considered that iron species were successfully loaded on the structure of MFBCs as

oxide particles. Additionally, it could be observed that MFBC-800 shown a significantly more porous structure than MFBC-500 and 650 (Figures S1), which was consistent with the results of BET (Table S1 and Figure S4). For the BBC, the specific surface area was 343.15 m^2/g, but after being modified by potassium ferrate, its surface area decreased to 0.662, 26.661, and 2.012 m^2/g in MFBC-500, MFBC-650, and MFBC-800, respectively. This may be due to the higher pore volume of biochar under higher temperature, which could load more iron species steadily (Figure S1) [32], and the increased load of iron species in turn reduced the specific surface area of MFBC. The HRTEM images shown the lattice structure of the MFBCs and BBC (Figures S3). The BBC exhibited an obvious regular lamellar structure with the lamellar spacing of 0.30 nm, indicating that graphitization happened on BBC (Figure S3a) [32, 33]. The 0.33 nm lattice gap of MFBC-800 should be attributed to lattice plane of Fe_3O_4 (Figure S3c) [34]. HRTEM image of MFBC-500 shown the d-placing of 0.22 nm, which was closed to lattice plane of Fe_2O_3 (104) (Figure S1a) [35]. Moreover, Figure S4a shown that the adsorption isotherm of BBC and MFBC-650 was type IV with H4 hysteresis loop, manifesting they had an incomplete and irregular pore structure. And the adsorption isotherm of MFBC- 800 was type II (Figure S4c and d), indicating the presence of larger pore sizes in the material [36].

Then, the crystal and graphite structures of the samples were analyzed by XRD. The XRD pattern is shown in Figure 1a, it could be seen that BBC exhibited a wide diffraction peak at 21.8°and 43.5°, which could be attributed to the amorphous structure

of pyrolysis induced graphite carbon. However, in MFBC, the peak of graphite carbon was weakened, indicating that the inherent carbon properties have changed significantly. And it also could be demonstrated that both MFBC-500, MFBC-650, and MFBC-800 showed the existence of iron oxide (Fe_2O_3, PDF #39-1346 and Fe_3O_4, PDF #65-3107). Diffraction peaks of 44.7° and 44.6° could be assigned to Fe^0 (PDF #65-4899). There was no significant difference between MFBC-500 and MFBC-650 in the composition of iron species, which may indicate that their ability to activate PI was similar. Meanwhile, a few different crystal forms of Fe_2O_3 were observed (e.g. PDF #47-1409 at 37.8° and 47.2°) in MFBC-800. Moreover, potassium was remained after the pyrolysis process, thus, in MFBC-800, the phase of K_3FeO_2 (PDF #48-0957) was also existed. Therefore, different temperature may lead to diverse interactions between potassium ferrate and biomass, higher temperature could lead to an increase in the diversity of iron species. The reference intensity ratio method (RIR) method was used to calculate the proportion of various iron species in MFBC-800 [37], the proportion of Fe_2O_3, Fe_3O_4, and Fe^0 in the XRD detection range was 72.2%, 7.6%, and 20.2%, respectively. In conclusion, biochar pyrolyzed at 800°C had a certain graphitized structure, and the weakening of graphite peak means that the biochar was coated with iron. Notably, higher pyrolysis temperature could introduce magnetic ferric oxide species (Fe_3O_4), which may enhance the magnetic properties of the materials, making them easier to recover from solution. Raman spectra of the three materials are shown in Figure 1b. The I_D/I_G was used to evaluate the degree of graphitization and defect

level in biochar-based materials [38]. Defects in the graphite carbon could lead to irregular structures, which could cause the I_D/I_G to rise. The highest I_D/I_G was observed for MFBC-800 (I_D/I_G = 1.16), followed by MFBC-500 (I_D/I_G = 1.06), MFBC-650 (I_D/I_G = 1.01), and BBC (I_D/I_G = 0.92). The similarity between MFBC-500 and MFBC-650 in defect degree indicated that the defect of MFBC could be formed under a certain high temperature. Moreover, the MFBC-800 had the highest defect degree in graphitized structure in the synthesized materials, which could be beneficial to produce active sites.

Surface chemical composition and iron species on MFBC-800 were further detected by XPS characterization. The high-resolution XPS spectra of C 1s and Fe 2p were analyzed, and the results were shown in Figures 1c and 1d. The C 1s spectrum can be deconvoluted into eight peaks (Figure 1c). The main peak at 248.8 eV could be attributed to sp^3 hybridized carbon atoms (C-C) [39]. The other seven peaks at 289.9 eV, 288.5 eV, 286.9 eV, 285.8 eV, 285.3 eV, 284.1 eV, and 283.0 eV could be ascribed to C=O (carbonyl or quinonyl), O=C-O (carboxyl or ester), C-N, C-O-C, C-OH, sp^2-bonded carbon (C=C), and Fe-C, respectively [40, 41]. The results also indicated that there were abundant types of functional groups on MFBC, such as C=O and C-N structures, which were of great significance for PI activation [42]. The Fe 2p spectrum of MFBC-800 could be deconvolved into three components (Figure 1d). Two peaks at 709.3 eV could be attributable to Fe(III), which were derived from iron species in the solid phase, suggesting the presence of Fe(III) species on the surface of MFBC-800 [43]. While the peaks at 708.5 and 707.5 eV could be assigned to the bound Fe(II) and

245 Fe^0, respectively [44]. The proportion of Fe^0 was 12.3%, while the proportion of Fe(III)
246 and Fe(II) was 25.3% and 62.4%, respectively. Since most of the activation of PI by Fe
247 starts from Fe(II), higher Fe(II) content means more active sites. Meanwhile, the
248 existence of Fe^0 may be attributed to the effect of reductive functional groups of biochar
249 on iron during pyrolysis [45]. More importantly, Fe^0 also played an important role in PI
250 activation according to previous studies [46].

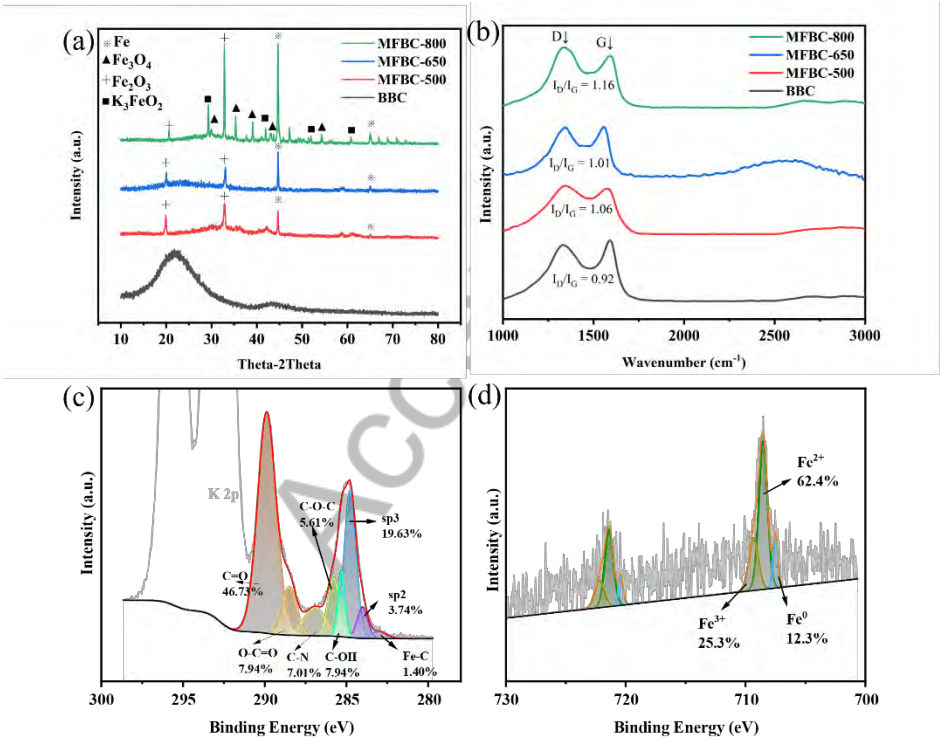

251

252 **Figure 1.** (a) XRD patterns of BBC and MFBCs; (b) Raman spectroscopy of BBC
253 MFBCs; (c) high-resolution XPS spectra of C 1s in MFBC-800; (d) high-resolution
254 XPS spectra of Fe 2p in MFBC-800.

255 **3.2 Degradation experiment of DDA**

256 3.2.1 Performance comparison of as-synthesized materials

257 MFBCs and BBC were used for DDA adsorption (Figure S5). MFBC-800 had the

best adsorption effect, reached equilibrium in 30 min, and removed about 25% of DDA. The adsorption performance of MFBC-650 was slightly lower than that of MFBC-800. Meanwhile, the adsorption ability of MFBC-500 to DDA in 60 min was not ideal, while the adsorption ability of BBC to DDA was even worse than that of MFBC-500.

The degradation of MFBC/PI system was shown that in the presence of PI, the degradation ratios of DDA by BBC, MFBC-500, MFBC-650, and MFBC-800 were 41.2%, 38.2%, 39.1%, and 97.9%, respectively (Figure 2a). The pseudo-first-order kinetic equation (Eq. 1) can be used to fit the DDA removal reaction well (Figure 2b).

$$\ln([DDA]_0/[DDA]_t) = k_{obs}t \quad (1)$$

$[DDA]_0$ and $[DDA]_t$ referred to the initial DDA concentration and DDA concentration at t min. The k_{obs} was the pseudo-first-order kinetic constant. The k_{obs} of MFBC-800/PI was about 6.1 times that of MFBC-500 and MFBC-650/PI (0.0613 min^{-1} to 0.0101 min^{-1} and 0.0104 min^{-1}), and about 4.8 times that of BBC/PI (0.0613 min^{-1} to 0.0129 min^{-1}). It was worth noting that, due to the very large specific surface area, the removal of DDA by BBC was possibly caused by adsorption. However, the available adsorption site for DDA is still lacking on BBC. Moreover, a slight rise (< 5%) in DDA in BBC happened after 15 min. This may be caused by desorption of PI, DDA, and by-products on limited adsorption sites in BBC [47-50]. Due to the small number of active species in BBC, DDA could not continue to be degraded after desorption. MFBC-500 has limited iron active sites and adsorption performance resulting in its very limited removal of DDA both by adsorption and PI activation. Due

279 to the higher surface area and iron-related sites in MFBC-650, the adsorption of DDA
280 was higher. However, the activation of MFBC-650 for PI still inhibited by low iron site
281 amount. Meanwhile, when there was only PI in the system, the removal of DDA within
282 60 min was less than 10%, indicating that PI could not degrade DDA effectively without
283 activation (Figure 2d). Overall, due to the excellent performance of MFBC-800, the
284 subsequent tests were carried out with MFBC-800. Figures 2c and d shown the effect
285 of PI/MFBC dosage on DDA removal. Under the condition that the dosage of MFBC-
286 800 was 0.1 g/L, 0.15 g/L, and 0.2 g/L, the degradation rates of DDA in 60 min were
287 72.6%, 87.9%, and 90.1%, respectively. When the dosage of PI was 0.5 g/L, 0.25 g/L,
288 and 0.1 g/L, the degradation rates of DDA were 99.9%, 90.1%, and 76.4% within 60
289 min, respectively. Furthermore, MFBC-800 retained more than 90% of DDA
290 degradation after the second reuse and 60% after the third reuse (Figure S6).
291 Considering the removal effect and reusability of DDA and the amounts of raw
292 materials used, in the subsequent experiments, the dosage of MFBC-800 and PI would
293 be set to 0.2 g/L and 0.25 g/L, respectively.

294 Furthermore, considering that the DDA adsorbed on MFBC may not be
295 degraded, the desorption experiment was carried out on the reacted MFBC (Text S4)
296 [51]. Almost no DDA was detected after 24 h of desorption. This result indicated that
297 the adsorbed DDA was almost completely degraded by MFBC activated PI-AOPs.

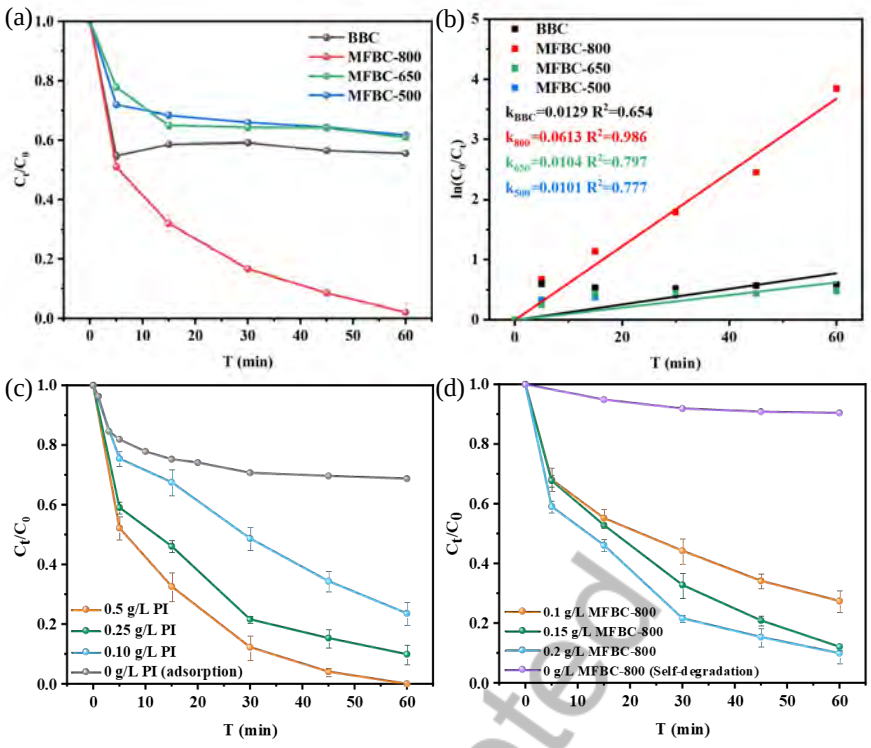

Figure 2. (a) Activate degradation of DDA by BBC/PI and MFBC/PI; (b) Pseudo-first order kinetics of BBC/PI and MFBC/PI; (c) Effect of PI dosage on degradation of DDA; (d) Effect of MFBC-800 dosage on degradation of DDA.

3.2.2 Effect of reaction parameters

As shown in Figure 3a, it was observed that the DDA removal efficiency of MFBC-800/PI system was almost the same at all pH values tested in the experiment, indicating the degradation ability of MFBC-800/PI system was relatively stable under acid and alkaline conditions. However, the removal effect of MFBC-800/PI on DDA was better at pH=3.0, and the k_{obs} reached 0.0594 min^{-1} (Figure 3c), which might be due to the production of higher redox potential radicals (such as •OH) under acidic conditions [52, 53]. Alternatively, the acidic environment improves the charging properties of the MFBC surface, making it more accessible to periodate ions for

311 efficient catalytic activation [9, 54]. In addition, it could be observed that in the first 5
312 min, the degradation of DDA at high pH was better than that at low pH. This could be
313 because: (a) an alkaline environment could induce PI activation and $^1O_2$ formation by
314 alkali. This pathway played a major role in DDA degradation in the first 5 min, while
315 the catalytic effect of MFBC was not significant [55]. After that, the pH rapidly returned
316 to neutral and reduced the alkali activation effect; (b) When the pH was low (pH = 5-
317 7), acidic environment reduced the positive charge of PI, thereby preventing it from
318 contacting the catalyst and reducing the activation efficiency [56, 57]. In general, pH
319 has no significant effect on the removal rate of DDA, which was consistent with
320 previous research [56, 58]. Furthermore, the pH of the mixture after the reaction was
321 measured. It was observed that the pH value of the reaction system will be stable near
322 neutral after 60 min of degradation experiment, no matter under acidic or alkaline
323 conditions (Table S2). Regarding this phenomenon, it may be due to the following
324 reasons: 1) under alkaline conditions, PI could be directly activated by HO^-, which in
325 turn produced $^1O_2$. Therefore, in this progress of $^1O_2$ production could be produced from
326 PI but not oxygen [7]. This was confirmed by the fact that DDA has the same
327 degradation effect either under N_2 or O_2 saturated conditions (Figure S7). In summary,
328 there was a phenomenon that PI and hydroxide directly produce $^1O_2$ in alkaline
329 environment, thereby leading to the decrease of pH; 2) when the system was in an acidic
330 environment, both the homogeneous phase reaction of iron leaching and the $^1O_2$
331 generation reaction initiated by $\bullet O_2^-$ could produce HO^- [9], thereby leading to the

increase of pH. Overall, the different activation pathways exhibited at different pH coincidentally led to the phenomenon that the MFBC/PI system maintained terminal pH close to neutral at a certain range of initial pH.

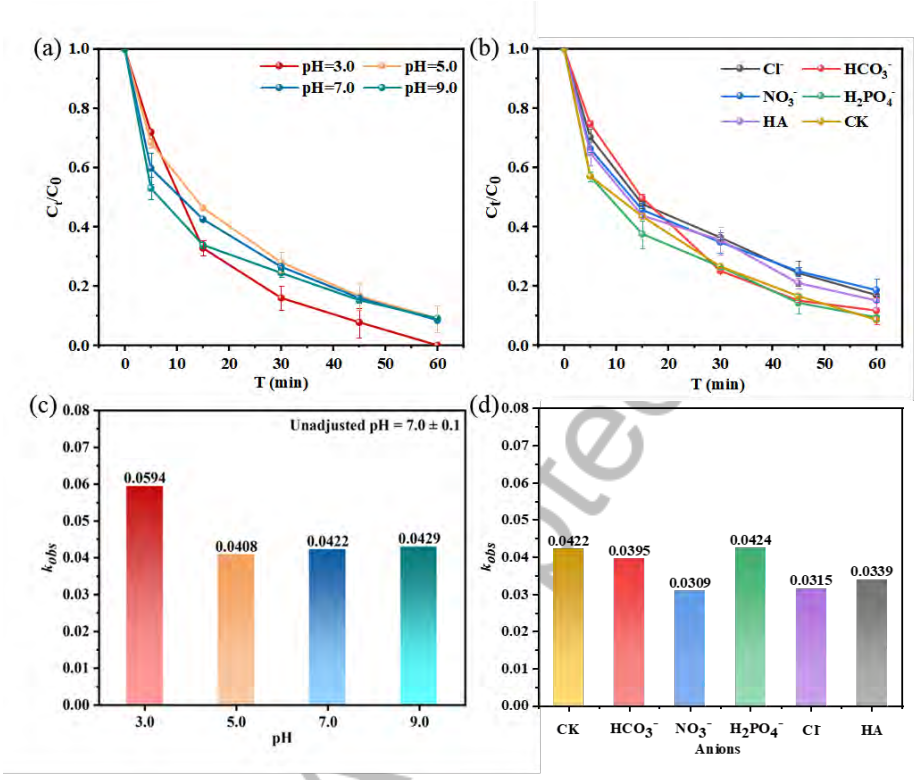

Figure 3. (a) Effect of initial pH to MFBC-800/PI system; (b) Effect of co-exist anions to MFBC-800/PI system; Influence of (c) pH and (d) anion on k_{obs}.

Without interfering ions, the pseudo first-order reaction rate k_{obs} was 0.0419 min^{-1} to MFBC-800/PI system, and $H_2PO_4^-$ had a slight promoting effect on the k_{obs} value (increased to 0.0424 min^{-1}). The HCO_3^-, HA, Cl^-, and NO_3^- all had a certain inhibitory effect, k_{obs} were 0.0395, 0.0339, 0.0339, and 0.0309 min^{-1}, respectively (Figures 3b and d). The results shown that anions except for $H_2PO_4^-$ had a negative effect on the reaction rate of MFBC/PI system. The HCO_3^- was a typical free radical scavenger, which had a strong effect on the dominant reaction of free radicals. Therefore, the mild inhibition of

bicarbonate may be due to its free radical scavenging effect as shown in Eqs. 2-5 [59-61]. The slight inhibition of Cl^- could be explained by the fact that it could react with IO_4^- with higher oxidation activity to form Cl• and IO_3^- with lower oxidation activity (shown in Eqs. 6-7) [54, 62]. Additionally, NO_3^- had a more significant inhibitory effect on DDA degradation than Cl^-. This inhibition could be due to the quenching of ROS by NO_3^-, which consumed ROS species and produced weakened reactive species (NO_3•) in the reaction system [63]. HA was reported to be a target compound during the oxidative degradation of organic pollutants [64]. Moreover, HA may adsorb on the surface of the catalyst and occupy the active site of the reaction. Therefore, HA interfered or competed with DDA degradation to a certain extent.

$$IO_4^- + HCO_3^- + H_2O \rightarrow IO_3\bullet + HCO_3\bullet + 2OH^- \quad (2)$$

$$HCO_3\bullet \leftrightarrow \bullet CO_3^- + H^+ \quad (3)$$

$$HCO_3^- + \bullet OH \rightarrow \bullet CO_3^- + H_2O \quad (4)$$

$$HCO_3^- + IO_3\bullet \rightarrow \bullet CO_3^- + IO_3^- + H^+ \quad (5)$$

$$IO_4^- + Cl^- + H_2O \rightarrow IO_3\bullet + Cl\bullet + 2OH^- \quad (6)$$

$$IO_3\bullet + Cl^- \rightarrow IO_3^- + Cl\bullet \quad (7)$$

In conclusion, the co-existence of anions and HA had a certain inhibitory effect on catalytic activation of PI by MFBC-800, but the inhibition effect was little. Therefore, the MFBC-800/PI system had high adaptability to the complex composition of mineral processing wastewater.

Furthermore, the degradation effect to DDA of MFBC/PI was verified in real water

366 (Table S3). High to 15 mg/L DDA was added to the real mineral wastewater to
367 MFBC/PI system to apply degradation. As shown in Figure S8, more than 90% of the
368 DDA was degraded by the MFBC/PI system even at a concentration of 15 mg/L,
369 indicating the ultra-high efficiency of the system in real water.

370 **3.3 Mechanism of PI/MFBC system**

371 3.3.1 Identification of active species in MFBC-800/PI system

372 To determine the contributing free radicals responsible for DDA degradation in
373 MFBC-800/PI system, radical quenching experiments were carried out. As shown in
374 Figure S9a, 50 mM MeOH (which can strongly quenching •OH) only reduced 6.3% of
375 DDA removal, indicating that •OH contributed little to the reaction [46, 65]. On the
376 contrary, quenching experiments with 50 mM L-Histidine (L-HIS) and 50 mM 2,2,6,6-
377 Tetramethyl-1-piperidinyloxy (TEMPO) were applied as quenchers to $^1O_2$ and $\bullet O_2^-$,
378 respectively. It was confirmed that L-HIS and TEMPO had significant inhibitory effects
379 on DDA removal. With the addition of L-HIS and TEMPO, the degradation rates of
380 DDA in 60 min were only 52.1% and 49.1%, respectively (Figure S9a). Therefore, $^1O_2$
381 and $\bullet O_2^-$ were important active species for DDA removal in MFBC-800/PI system [66].
382 Based on the above analyses, it could be concluded that $^1O_2$ and $\bullet O_2^-$ played a leading
383 role in the removal of DDA in MFBC-800/PI system. Additionally, $IO_3\bullet$ was widely
384 believed to exist in PI based AOP [9, 59]. EPR was used to verify the presence of $IO_3\bullet$.
385 As shown in Figure S10, spectral width (SW) was about 41G, and the hyperfine
386 coupling constants were 12.8 (A_H) and 14.5 (A_N), which could be identified as the

characteristic spectrum of IO_3•. The IO_4• signal was also present but very weak [67].

Structure-activity relationship and coupling effect of biochar

Firstly, the role of carbon structure of MFBC-800 material in the system of MFBC/PI was explored. FTIR spectra were used for discussing the function of the functional group in biochar (before and after use) in PI activation. The FTIR spectra of raw MFBC-800 was shown in Figure 4a. Peaks of functional groups are listed in Table S4. Functional groups including O-H, C-H, C=O, C=C, C-O, O-C-O, and C-N were determined by FTIR, which was consistent with the results of XPS (Figure 1b) [1, 68]. For the FTIR image of used MFBC-800 (Figure 4a), only O-H, C=C, C-N, and some peaks of C-H were detected (Table S4). Additionally, XPS spectra of MFBC-800 (after reuse, Figure S9e) shown that the ratio of C=O decreased from 46.73% to 2.35% and O-C=O decreased from 7.94% to 4.81%, while the ratio of C-O species increased from 13.55% to 22.94% and sp3 C increased from 19.63% to 58.82% after the reaction. However, no meaningful changes were observed in the ratio of C-N functional group. In conclusion, C=O may significantly promote PI activation to produce active species ($^1O_2$), then self-decay to other function groups or carbon skeleton, which was consistent with the previous studies [42]. Furthermore, •OH was contributed only a limited amount to DDA degradation through the quenching experiment, while •OH was confirmed related to the defect degree of biochar in previous studies [69]. Therefore, it indicated that the defect degree of biochar does not play a decisive role in PI activation.

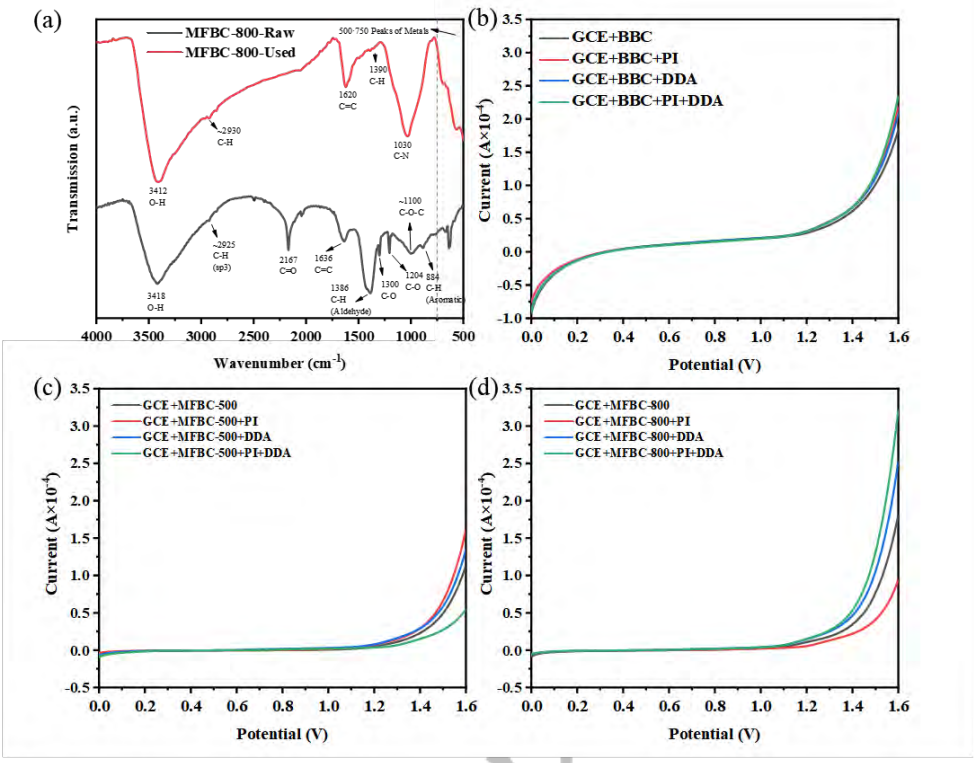

407

408 **Figure 4.** FT-IR pattern of (a) raw MFBC-800 and used MFBC-800; LSV curves of (b)

409 BBC, (c) MFBC-500, and (d) MFBC-800 and their combined system.

410 Secondly, the electron shuttle process of the MFBC-800 system was analyzed by

411 analyzing the linear sweep voltammogram (LSV), and then the redox process of the

412 MFBC-800/PI system was evaluated. The LSV curves BBC had no significant response

413 to the addition of PI or DDA (Figure 4b). MFBC-500 shown weaker electron transfer

414 after adding PI and DDA (Figure 4c). Notably, after DDA addition, the electrical

415 conductivity increased significantly, indicating the existence of interface electron

416 transfer from DDA to MFBC-800 (Figure 4d). This might suggest that MFBC-800 acted

417 as an electron shuttle to facilitate the transfer of electrons from DDA to PI, thereby

418 promoting the oxidation of DDA through a non-radical mechanism.

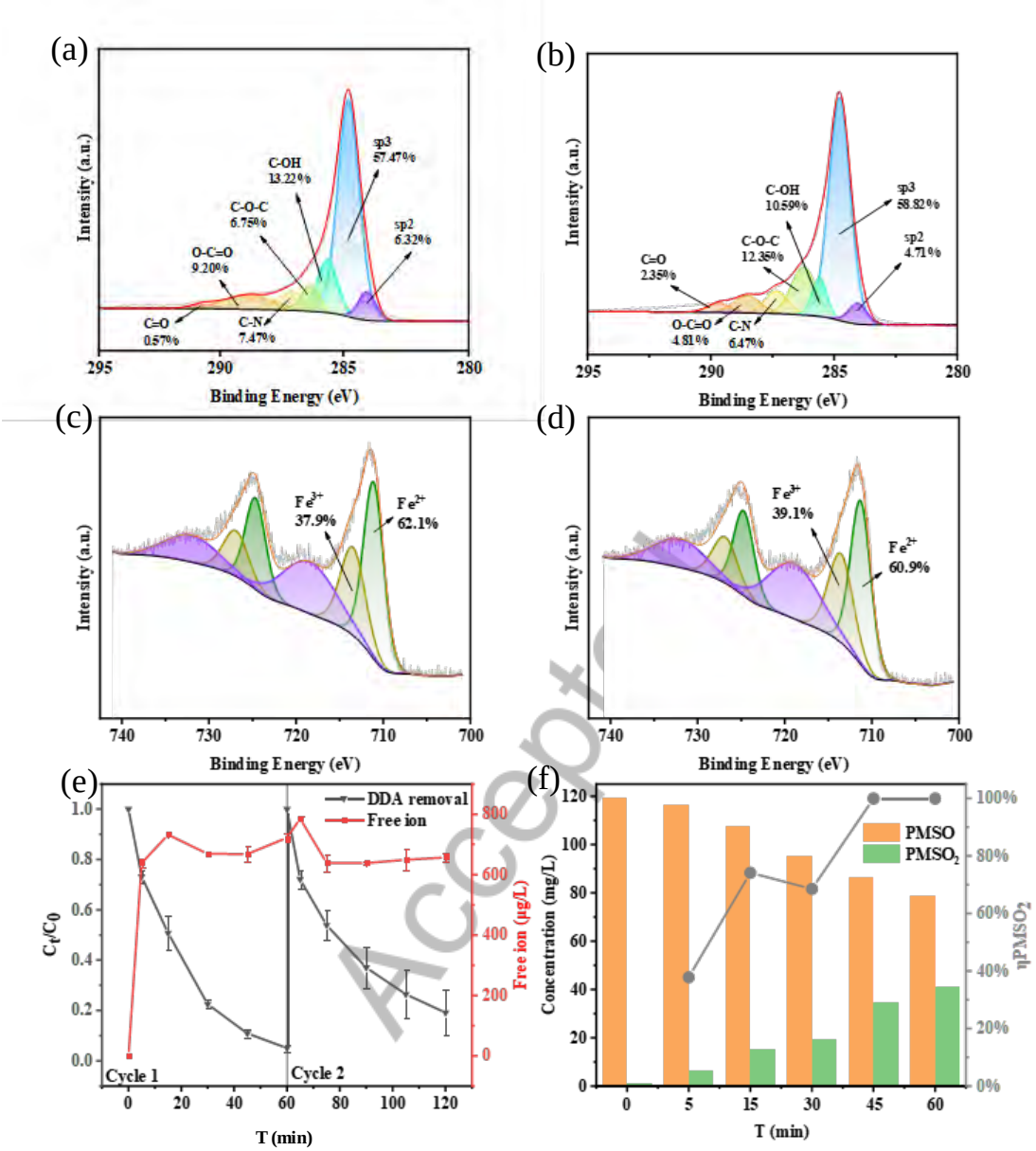

419

420 **Figure 5.** XPS high-resolution spectrum of used MFBC-800: (a) C 1s after cycle 1, (b)

421 C 1s after cycle 2, (c) Fe 2p after cycle 1, (d) Fe 2p after cycle 2, and (e) DDA removal

422 and free total iron in cycle experiments; (f) PMSO and $PMSO_2$ amount during reaction.

423 3.3.2 Behaviors of iron species at the solid-liquid interface

424 Leaching of Fe was expected because the binding of Fe to biochar was not very

425 strong. In addition, PI-AOPs were different from Fenton or persulfate oxidation. In the

426 reaction process, the pH would be close to neutral, which was also conducive to the

precipitation of Fe on biochar surface. Therefore, the existence form of Fe species was very complex and there was frequent morphological transformation between them. Using the solid-liquid interface as a background for studying the behavior of Fe species could help to understand the leaching-precipitation cycle, the redox cycle, and the generation of iron-active species.

Firstly, for most advanced oxidation reactions involving transition metals, the metal redox cycle must exist [70, 71]. It could be seen that Fe^0 on the surface of the material was not detected after reaction (Figure 5c), and the ratio of Fe(II) to Fe(III) decreased after cycle 1 (Figures 1b and 5c). This phenomenon might be caused by the transformation of Fe^0 to Fe(II), then Fe(II) rapidly activated PI and was converted to Fe(III). Furthermore, XPS spectra of MFBC-800 (after cycle 1 and cycle 2) shown that the proportion of Fe in different valence states on the surface of the material had little change (Figures 5c and d). This result indicated that iron species were more likely to undergo iron cycling in the liquid phase in the form of free iron. In addition, the changes of Fe(II) and Fe(III) species between cycle 1 and cycle 2 were slight, indicating that the redox cycle of Fe was in equilibrium during the activation process.

Due to the unique characteristic of PI-AOPs keeping pH close to neutral, the iron leaching cycle was an important process. Iron leaching-precipitation was determined by measuring the free iron content in the reaction solution samples collected during the continuous degradation experiment. The content of free iron remained stable in the range of 638~785 μg/L (Figure 5e). Especially after 15 min of cycle 2, the free iron

content was maintained at 640 μg/L, indicating that the iron leaching-precipitation process at the material-liquid interface was balanced at this time. The reuse experiments further demonstrated the leaching-precipitation equilibrium of the MFBC/PI system. In the reuse experiments, the efficiency of the MFBC/PI system was significantly reduced. Because previous Fe ions-containing reaction fluid was discarded and the new DDA solution was used for the reaction. This process disrupted the leaching-precipitation equilibrium, causing the MFBC to release Fe in a new turn of reuse.

Fe(IV) could be generated during PI homogeneous catalysis, which could degrade pollutants as an active species. For MFBC with iron leaching-precipitation cycles, Fe(IV) was likely to be present. It could be seen from the above equations that Fe(IV) was an important driving factor for MFBC/PI. Since Fe(IV) could be oxidized selectively by methyl phenyl sulfoxide (PMSO) to methyl phenyl sulfone ($PMSO_2$), PMSO was added to MFBC/PI system and single-PI system to determine the formation of Fe(IV) [72]. As shown in Figure 5f, in the single-PI system, the content of PMSO decreased rapidly in the first 5 min, while in the MFBC-800/PI system, PMSO decreased at a constant ratio throughout the reaction process. More importantly, for the single-PI system, there was almost no $PMSO_2$ formation, whereas for the MFBC-800/PI system, $PMSO_2$ was steadily generated within 60 min. Figure 5f presents the yield of $PMSO_2$ ($\eta PMSO_2$). In the first 5 min, the yield of $PMSO_2$ is less than 40%, which could be due to the low concentration of free Fe(II) in the solution (Figure 5e), thereby there was not enough Fe(IV) to generate $PMSO_2$ from PMSO. During this time,

fewer reactive species were produced in MFBC/PI and most of the consumed PMSO was reacted with other oxidizing species such as radicals. From 5 to 15 min, free Fe(II) leached from Fe(II) and Fe^0 activated PI and generated Fe(IV), thereby This resulted in an increasing $PMSO_2$ yield. At 30 min, the yield of $PMSO_2$ decreased slightly, suggesting that the free iron leaching and redox cycling at the interface were in equilibrium, which was consistent with Figure 5e. After 30 min, the yield of $PMSO_2$ was 100%, indicating that the main reactive species produced by MFBC/PI system at this time was Fe(IV). Meanwhile, almost no $PMSO_2$ was generated in the PI-only system (Figure S11a). Therefore, two possible facts have been confirmed by PMSO conversion experiments: (a) Fe(VI) does exist in the MFBC/PI system, and (b) the leaching-iron from the material surface to the solid-liquid interface was the main reason limiting the rate of Fe(IV) production. More interestingly, when DDA was added to the MFBC/PI system with PMSO probe, both PMSO consumption and $PMSO_2$ production were significantly inhibited to a negligible level (Figure S11b). This indicated that Fe(IV) produced by the MFBC/PI system and its subsequent products of the active species chain reaction were used to degrade DDA. Therefore, Fe(IV) was existed and its generation was continuous in the MFBC/PI system. The main product of Fe(IV) self-decay, H_2O_2, has also been shown to exist by iodometry (Text S3). When potassium hydrogen phthalate and potassium iodide were added to the solution after reaction, the solution showed an absorption peak at about 351 nm (Figure S12a). Additionally, activated PI with free iron (0.6 mg/L) had a certain effect on DDA degradation (about

50%, Figure S12b), but after the rapid degradation in the first 5 min, DDA degradation almost stopped. Therefore, compared with leaching-iron, the MFBC/PI heterogeneous system had the advantage of efficient and continuous in the degradation progress of DDA.

In summary, the mechanism of iron activation can be further subdivided into two branches: (a) Fe^0 on MFBC-800 triggered PI activation (Eq. 8), large amounts of iodate radical and Fe(II) were produced [9]; (b) the production of $\bullet O_2^-$ and Fe(IV) caused by Fe(II) (Eqs. 9-10, Fe(IV)=O was the main form of Fe(IV)) [9, 73].

$$Fe^0 + 2IO_4^- + H^+ \rightarrow Fe(II) + 2IO_3\bullet + 2OH^- \quad (8)$$

$$Fe(II) + IO_4^- + H_2O \rightarrow Fe(III) + IO_3^- + \bullet O_2^- + 2H^+ \quad (9)$$

$$Fe(II) + IO_4^- \rightarrow Fe(IV)=O + IO_3^- \quad (10)$$

In addition, the Fenton-like processes was produced by the Fe(II) and H_2O_2 (Eq. 11), which may be the main formation mode of •OH, and the regeneration of Fe(II) or Fe(III) from Fe(IV) by the following mechanisms [9]:

$$2Fe(IV) \rightarrow 1/3H_2O_2 + 2Fe(III) + 1/3O_2 \text{ (Self-decay of Fe(IV))} \quad (11)$$

In Fenton or Fenton-like systems, the electron transfer system formed by Fe(III)-H_2O_2 to regenerate Fe(II), providing a more sustained degradation capacity than the homogeneous reactions [9, 74]:

$$Fe(III) + H_2O_2 \rightarrow Fe(II) + \bullet O_2^- + 2H^+ \quad (12)$$

The formation of $^1O_2$ by radical chain reaction and provide the basicity [46, 73]:

$$IO_4^- + 2\bullet O_2^- + H_2O \rightarrow IO_3^- + 2OH^- + 2^1O_2 \quad (13)$$

$$2\bullet O_2^- + H_2O \rightarrow H_2O_2 + {}^1O_2 + 2OH^- \quad (14)$$

The final degradation of DDA was carried out through Eq. 15:

$$Fe(IV)/{}^1O_2/\bullet O_2^-/IO_3\bullet + DDA \rightarrow \text{Degradation products} \quad (15)$$

Finally, the synergistic effect of biochar and iron-loaded species in activating PI was analyzed. Mainly divided into the following two aspects: (a) due to the adsorption of biochar, DDA was adsorbed to the surface/pore of biochar, thus increasing the contact reaction surface between iron oxide and DDA to a large extent; (b) Fe(II) can be connected with BC-O• to form BC-O•-Fe(II), and then reacted with H_2O_2 to produce •OH and BC=O or BC-O-Fe(III), which further increased the reaction activity and degradation efficiency of the system to a certain extent. Fe(III) in solid phase was dominant in the MFBC-used according to XPS (Figure 5c-d and S9f). Combined with Figures 5c and d, the activation mechanism on the iron-bearing carbon skeleton can be determined mainly through Fe(II) conversion to Fe(III) as shown in Eq.16 [11].

$$\text{BC-O•-Fe(II)} + H_2O_2 \rightarrow \text{BC-O-Fe(III)} + \bullet OH \quad (16)$$

The contribution of soluble iron and DOM on the MFBC in PI activation was shown in Figure S12c. This result indicated that the contribution of leaching iron and DOM to PI activation was few. In conclusion, the activation mechanism of MFBC-800/PI system was complex, iron and biochar can act independently in this process, but also had a synergistic effect to some extent. The above mechanism was shown in Figure 6.

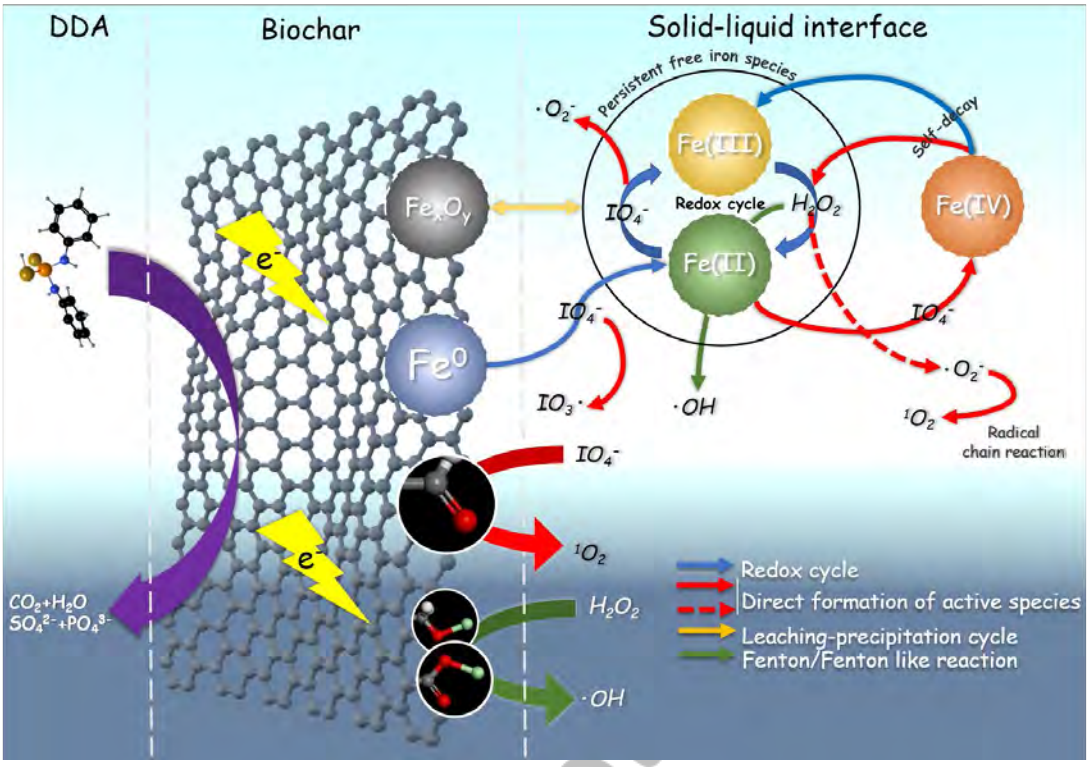

Figure 6. Mechanism of DDA degradation in MFBC/PI system.

3.4 Identification of degradation products

3.4.1 Identification of iodine species

PI-AOPs may produce a range of iodine species, including I_2, HOI, IO_3^-, IO_4^-, and I^-. Thus, iodine by-products were identified. As shown in Figure S13a, the reaction solution after the addition of starch did not turn to blue, indicating that I_2 was not generated. Chromatograms of phenol degradation in MFBC/PI system are shown in Figure S13b. There was no 2-IP or 4-IP at 8.0 or 8.8 min except for the quencher and phenol peaks at 2.0 min or 6.3 min, respectively. This indicated that MFBC/PI did not produce detectable HOI. Finally, Figure S13c shown the transformation from IO_4^- to IO_3^- but KI peak was not detected, indicating that IO_3^- was the main by-product of MFBC/PI system. In conclusion, the MFBC/PI system did not produce iodine by-

544 products with high environmental risks.

545 3.4.2 Identification of DDA by-products

546 Possible attack sites on DDA were evaluated using Fukui Index (Table 1 and
547 Figure S14). f^0 was used to evaluate attack of radical ($\bullet O_2^-$/$IO_3\bullet$/$\bullet OH$). The 1(P), 2(S),
548 3(S), 9(C), 15(C) sites had large f^0, making it a free radical attack site. Condensed dual
549 descriptor (CDD) was suitable for evaluate $^1O_2$ attack trend. A negative CDD indicated
550 greater vulnerability to electrophilic reagents, such as $^1O_2$ and Fe(IV)=O [75, 76]. 3(S),
551 4(N), 5(N), 6(C), 7(C), 9(C) tend to be attacked by $^1O_2$ and Fe(IV)=O.

552 **Table 1. Fukui index and CDD of DDA.**

Atom	q(N)	q(N+1)	q(N-1)	f^-	f^+	f^0	CDD
1(P)	0.3703	0.2942	0.3847	0.0144	0.0761	0.0453	0.0617
2(S)	-0.0972	-0.3083	-0.0354	0.0618	0.2112	0.1365	0.1494
3(S)	-0.3403	-0.5031	-0.1591	0.1812	0.1629	0.172	-0.0183
4(N)	-0.1415	-0.1536	-0.1055	0.036	0.0121	0.024	-0.0239
5(N)	-0.1464	-0.1535	-0.0974	0.0491	0.0071	0.0281	-0.042
6(C)	0.0445	0.0385	0.0687	0.0242	0.006	0.0151	-0.0182
7(C)	-0.0564	-0.0614	-0.0318	0.0246	0.005	0.0148	-0.0197
8(C)	-0.0353	-0.0617	-0.0056	0.0297	0.0264	0.0281	-0.0033
9(C)	-0.0494	-0.0861	0.0137	0.0631	0.0367	0.0499	-0.0265
10(C)	-0.0381	-0.0608	-0.0043	0.0339	0.0227	0.0283	-0.0112
11(C)	-0.0579	-0.0815	-0.0237	0.0343	0.0236	0.0289	-0.0107

12(C)	0.0414	0.026	0.0636	0.0223	0.0154	0.0188	-0.0068
13(C)	-0.059	-0.0687	-0.0368	0.0222	0.0097	0.016	-0.0126
14(C)	-0.0357	-0.0684	-0.0092	0.0264	0.0327	0.0296	0.0063
15(C)	-0.0485	-0.0984	0.0089	0.0574	0.0499	0.0536	-0.0075
16(C)	-0.0376	-0.0648	-0.0052	0.0324	0.0272	0.0298	-0.0052
17(C)	-0.0576	-0.0903	-0.0276	0.03	0.0327	0.0314	0.0028

Meanwhile, degradation intermediates of DDA in MFBC/PI system were determined by GC-MS (Figures 7a and S15). First, the 1(P) on DDA was attacked by free radicals generated in the MFBC/PI system, leading to the formation of aniline (P1), the remaining phosphoric acid continued to be oxidized to sulfur dioxide and nitrogen dioxide [27]. N-radical coupling of aniline radicals lead to the formation of P2, which was then converted to P3 by electrophilic addition and ring-opening reaction [77]. The amino or benzene ring of P1 was then attacked by •OH or $•O_2^-$ to form nitrobenzene (P4) and phenol (P5) [78, 79]. The aromatic ring is attacked by free radicals, leading to the production of aniline radical intermediates, which react with aniline to form 4, 4-benzidine (P6) or N-Phenyl-p-phenylenediamine (P7) [80]. The complex radical chain-growth reaction and ring opening reactions eventually lead to the formation of long-chain byproducts (such as P8 and P9) and their further oxidation [81, 82]. Despite the generation of a series of by-products, the MFBC/PI system possessed a better mineralization ability, removing 50% of TOC within 60 min.

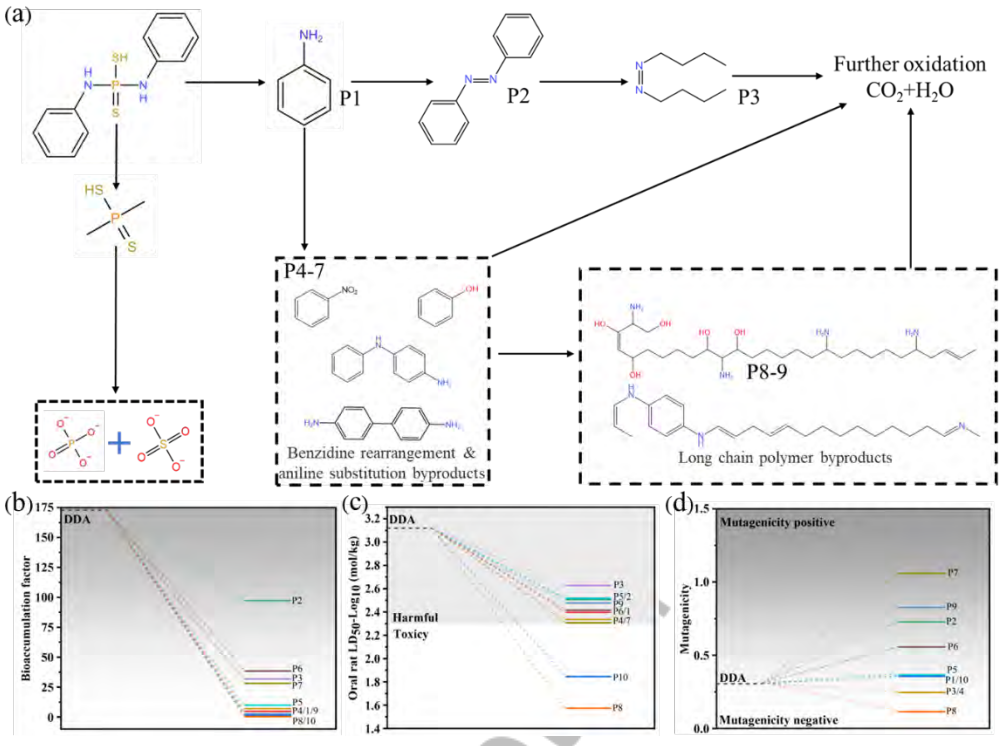

Figure 7. (a) The degradation pathway and by-products of DDA; (b) Bioaccumulation factor of degradation by-products of DDA; (c) Oral rat LD_{50}-Log_{10} degradation by-products of DDA; (d) Mutagenicity of DDA degradation by-products.

3.5 Toxicity levels of intermediate products

The toxicity of the MFBC-800/PI system for DDA degradation was evaluated by Toxicity Estimation Software Tool (T.E.S.T), where three different toxicity indexes including bioaccumulation factor, Oral rat LD50, and mutagenicity were investigated based on the quantitative structure-activity relationship (QSAR) analyses [83]. As shown in Figure 7b, MFBC-800/PI system can significantly reduce the bioaccumulation factor for almost all the intermediates. Additionally, DDA and most of the intermediates with an oral rat LD_{50} belong to the "harmful" level, while the P8 and P10 belong to the "Toxicity" level. However, the P10 would be degraded to PO_4^{3-} and

580 SO_4^{2-} (non-toxicity) immediately, and the bioaccumulation index of P8 was very low,
581 which had limited influence on the whole ecological chain (Figure 7c). As shown in
582 Figure 7d, DDA was a mutagenic negative chemical. After the degradation, the
583 mutagenicity of most of the intermediates increased slightly. In conclusion, MFBC-
584 800/PI could partially transform DDA into non-toxic inorganic substances. Although
585 there were intermediates with relatively high toxicity, almost all of them would
586 continuously oxidize or have poor bioaccumulation.

587 **4 Environmental Implications**

588 The magnetic ferrite-modified biochar (MFBC) prepared in this study are effective
589 PI activators for the degradation of DDA through multiple active species (Fe(IV), $^1O_2$,
590 $\bullet O_2^-$, and $IO_3\bullet$). The PI can be activated by Fe^0, Fe(II), and the functional groups of
591 biochar (especially C=O), thus generating $\bullet O_2^-$, $^1O_2$, $IO_3\bullet$, and Fe(IV). The iron
592 leaching-precipitation cycles and iron redox cycles played important role in the
593 degradation process. Phosphorus atoms and sulfur atoms on DDA seem to be the main
594 active sites in MFBC/PI systems. Notably, the leaching rate of iron ions remained at a
595 low level during the degradation process. The PI/MFBC system maintained stable
596 efficiency under wide pH ranges and the presence of various interfering anions. The
597 findings of this study may provide some guidance for the application of iron-carbon
598 composites as a green catalyst in the advanced PI-based oxidation process. However,
599 how to regulate the radical pathway and non-radical pathway in PI activation, how to
600 utilize the defect sites of biochar, and the detailed mechanism of pH effects in

601 heterogeneous PI-AOPs systems still need further research.

602

Acknowledgements

This research was financially supported by the National Natural Science Foundation of China (U20A20323), the National Key R&D Program of China (2020YFC1807600), the Program for Changjiang Scholars and Innovative Research Team in University (IRT-13R17), the Natural Science Foundation of Hunan Province, China (2021JJ30123), the Science and Technology Innovation Program of Hunan Province (2021RC2057), the Project funded by China Postdoctoral Science Foundation (2021M700041), the National Natural Science Foundation of Changsha (kq2202166).

References:

[1] J. Sirvio, U. Hyvakko, H. Liimatainen, J. Niinimaki, O. Hormi, Periodate oxidation of cellulose at elevated temperatures using metal salts as cellulose activators, Carbohyd Polym, 83 (2011) 1293-1297.

[2] C. Lee, J. Yoon, Application of photoactivated periodate to the decolorization of reactive dye: reaction parameters and mechanism, Journal of Photochemistry and Photobiology A: Chemistry, 165 (2004) 35-41.

[3] M. Yang, Z. Hou, X. Zhang, B. Gao, Y. Li, Y. Shang, Q. Yue, X. Duan, X. Xu, Unveiling the Origins of Selective Oxidation in Single-Atom Catalysis via Co–N4–C Intensified Radical and Nonradical Pathways, Environmental Science & Technology, 56 (2022) 11635-11645.

[4] D. Kanakaraju, B.D. Glass, M. Oelgemöller, Advanced oxidation process-mediated removal of pharmaceuticals from water: A review, Journal of Environmental Management, 219 (2018) 189-207.

[5] P. Cai, J. Zhao, X. Zhang, T. Zhang, G. Yin, S. Chen, C.-L. Dong, Y.-C. Huang, Y. Sun, D. Yang, B. Xing, Synergy between cobalt and nickel on NiCo2O4 nanosheets promotes peroxymonosulfate activation for efficient norfloxacin degradation, Appl Catal B-Environ, 306 (2022) 121091.

[6] Y. Shang, X. Liu, Y. Li, Y. Gao, B. Gao, X. Xu, Q. Yue, Boosting fenton-like reaction by reconstructed single Fe atom catalyst for oxidizing organics: Synergistic effect of conjugated π-π sp2 structured carbon and isolated Fe-N4 sites, Chemical Engineering Journal, 446 (2022) 137120.

[7] A.D. Bokare, W. Choi, Singlet-Oxygen Generation in Alkaline Periodate Solution, Environmental Science & Technology, 49 (2015) 14392-14400.

[8] Y. Choi, H.I. Yoon, C. Lee, L. Vetrakova, D. Heger, K. Kim, J. Kim, Activation of Periodate by Freezing for the Degradation of Aqueous Organic Pollutants, Environmental Science & Technology, 52 (2018) 5378-5385.

[9] Y. Zong, Y. Shao, Y. Zeng, B. Shao, L. Xu, Z. Zhao, W. Liu, D. Wu, Enhanced Oxidation of Organic Contaminants by Iron(II)-Activated Periodate: The Significance of High-Valent Iron-Oxo Species, Environmental Science & Technology, 55 (2021) 7634-7642.

[10] F. Liu, Z. Li, Q. Dong, C. Nie, S. Wang, B. Zhang, P. Han, M. Tong, Catalyst-Free Periodate Activation by Solar Irradiation for Bacterial Disinfection: Performance and Mechanisms, Environmental Science & Technology, 56 (2022) 4413-4424.

[11] G. Fang, J. Li, C. Zhang, F. Qin, H. Luo, C. Huang, D. Qin, Z. Ouyang, Periodate activated by manganese oxide/biochar composites for antibiotic degradation in aqueous system: Combined effects of active manganese species and biochar, Environmental Pollution, 300 (2022) 118939.

[12] H. Kim, H.-Y. Yoo, S. Hong, S. Lee, S. Lee, B.-S. Park, H. Park, C. Lee, J. Lee, Effects of inorganic oxidants on kinetics and mechanisms of WO 3 -mediated photocatalytic degradation, Appl Catal B-Environ, 162 (2015) 515-523.

[13] H. Ye, S. Liu, D. Yu, X. Zhou, L. Qin, C. Lai, F. Qin, M. Zhang, W. Chen, W. Chen, L. Xiang, Regeneration mechanism, modification strategy, and environment application of layered double hydroxides: Insights based on memory effect, Coordination Chemistry Reviews, 450 (2022) 214253.

[14] J. Wang, F. Xu, H. Jin, Y. Chen, Y. Wang, Non-Noble Metal-based Carbon Composites in Hydrogen Evolution Reaction: Fundamentals to Applications, Advanced Materials, 29 (2017) 1605838.

[15] L. Jiao, Y. Wang, H.L. Jiang, Q. Xu, Metal-Organic Frameworks as Platforms for Catalytic Applications, Advanced Materials, 30 (2018) e1703663.

[16] T. Do Minh, J. Song, A. Deb, L. Cha, V. Srivastava, M. Sillanpää, Biochar based catalysts for the abatement of emerging pollutants: a review, Chemical Engineering Journal, 394 (2020) 124856.

[17] F. Qin, J. Li, C. Zhang, G. Zeng, D. Huang, X. Tan, D. Qin, H. Tan, Biochar in the 21st century: A data-driven visualization of collaboration, frontier identification, and future trend, Science of the Total Environment, 818 (2022) 151774.

[18] G. Fang, C. Liu, J. Gao, D.D. Dionysiou, D. Zhou, Manipulation of persistent free radicals in biochar to activate persulfate for contaminant degradation, Environmental Science & Technology, 49 (2015) 5645-5653.

[19] Z. Chen, J. Yao, T. Šolević Knudsen, B. Ma, B. Liu, H. Li, X. Zhu, C. Zhao, W. Pang, Y. Cao, Degradation of novel mineral flotation reagent 8-hydroxyquinoline by superparamagnetic immobilized laccase: Effect, mechanism and toxicity evaluation, Chemical Engineering Journal, 432 (2022) 134239.

[20] Y.-L. Zhang, W.-L. Wang, M.-Y. Lee, Z.-W. Yang, Q.-Y. Wu, N. Huang, H.-Y. Hu, Promotive effects of vacuum-UV/UV (185/254 nm) light on elimination of recalcitrant trace organic contaminants by UV-AOPs during wastewater treatment and reclamation: A review, Science of the Total Environment, (2021) 151776.

[21] E. Issaka, J.N.-O. Amu-Darko, S. Yakubu, F.O. Fapohunda, N. Ali, M. Bilal, Advanced catalytic ozonation for degradation of pharmaceutical pollutants—A review, Chemosphere, 289 (2022) 133208.

[22] W. Lin, S. Sun, C. Wu, P. Xu, Z. Ye, S. Zhuang, Effects of toxic organic flotation reagent (aniline aerofloat) on an A/O submerged membrane bioreactor (sMBR): Microbial community dynamics and performance, Ecotoxicology and Environmental Safety, 142 (2017) 14-21.

[23] L. Xiang, T. Xiao, C.-H. Mo, H.-M. Zhao, Y.-W. Li, H. Li, Q.-Y. Cai, D.-M. Zhou, M.-H. Wong, Sorption kinetics, isotherms, and mechanism of aniline aerofloat to agricultural soils with various physicochemical properties, Ecotoxicology and Environmental Safety, 154 (2018) 84-91.

[24] N.K. Chaturvedi, Comparison of available treatment techniques for hazardous aniline-based organic contaminants, Applied Water Science, 12 (2022) 1-15.

[25] Z. Tan, C.S.K. Lin, X. Ji, T.J. Rainey, Returning biochar to fields: A review, Applied Soil Ecology, 116 (2017) 1-11.

[26] M. Fu, J. Huang, S. Feng, T. Zhang, P.-C. Qian, W.-Y. Wong, One-step solid-state pyrolysis of bio-wastes to synthesize multi-hierarchical porous carbon for ultra-long life supercapacitors, Materials Chemistry Frontiers, 5 (2021) 2320-2327.

[27] W. Lin, J. Tian, J. Ren, P. Xu, Y. Dai, S. Sun, C. Wu, Oxidation of aniline aerofloat in flotation wastewater by sodium hypochlorite solution, Environmental Science And Pollution Research, 23 (2016) 785-792.

[28] R. Dennington, T.A. Keith, J.M. Millam, S. Inc., Gaussview, Shawnee Mission, KS, 2016.

[29] M.J. Frisch, G.W. Trucks, H.B. Schlegel, G.E. Scuseria, M.A. Robb, J.R. Cheeseman, G. Scalmani, V. Barone, G.A. Petersson, H. Nakatsuji, X. Li, M. Caricato, A.V. Marenich, J. Bloino, B.G. Janesko, R. Gomperts, B. Mennucci, H.P. Hratchian, J.V. Ortiz, A.F. Izmaylov, J.L. Sonnenberg, Williams, F. Ding, F. Lipparini, F. Egidi, J. Goings, B. Peng, A. Petrone, T. Henderson, D. Ranasinghe, V.G. Zakrzewski, J. Gao, N. Rega, G. Zheng, W. Liang, M. Hada, M. Ehara, K. Toyota, R. Fukuda, J. Hasegawa, M. Ishida, T. Nakajima, Y. Honda, O. Kitao, H. Nakai, T. Vreven, K. Throssell, J.A. Montgomery Jr., J.E. Peralta, F. Ogliaro, M.J. Bearpark, J.J. Heyd, E.N. Brothers, K.N. Kudin, V.N.

Staroverov, T.A. Keith, R. Kobayashi, J. Normand, K. Raghavachari, A.P. Rendell, J.C. Burant, S.S. Iyengar, J. Tomasi, M. Cossi, J.M. Millam, M. Klene, C. Adamo, R. Cammi, J.W. Ochterski, R.L. Martin, K. Morokuma, O. Farkas, J.B. Foresman, D.J. Fox, Gaussian 16 Rev. A.03, Wallingford, CT, 2016.

[30] T. Lu, F. Chen, Multiwfn: a multifunctional wavefunction analyzer, Journal of Computational Chemistry, 33 (2012) 580-592.

[31] C. Yang, Z. Yang, K. Yang, Z. Yu, Y. Zuo, L. Cheng, Y. Wang, H. Sun, G. Yu, C. Zhang, X. Li, Periodate activated by different crystalline phases MnO2 for profound oxidation tetracycline hydrochloride: Oxygen vacancy-dominated active pivots and mechanism, Separation and Purification Technology, 301 (2022) 122022.

[32] S. Ye, M. Yan, X. Tan, J. Liang, G. Zeng, H. Wu, B. Song, C. Zhou, Y. Yang, H. Wang, Facile assembled biochar-based nanocomposite with improved graphitization for efficient photocatalytic activity driven by visible light, Appl Catal B-Environ, 250 (2019) 78-88.

[33] Q. Yan, C. Wan, J. Liu, J. Gao, F. Yu, J. Zhang, Z. Cai, Iron nanoparticles in situ encapsulated in biochar-based carbon as an effective catalyst for the conversion of biomass-derived syngas to liquid hydrocarbons, Green Chem, 15 (2013) 1631-1640.

[34] Z. Wu, H. Yu, L. Kuai, H. Wang, T. Pei, B. Geng, CdS urchin-like microspheres/alpha-Fe2O3 and CdS/Fe3O4 nanoparticles heterostructures with improved photocatalytic recycled activities, Journal of Colloid and Interface Science, 426 (2014) 83-89.

[35] C.C. Li, R.J. Lin, H.P. Lin, Y.K. Lin, Y.G. Lin, C.C. Chang, L.C. Chen, K.H. Chen, Catalytic performance of plate-type Cu/Fe nanocomposites on ZnO nanorods for oxidative steam reforming of methanol, Chem Commun (Camb), 47 (2011) 1473-1475.

[36] K.S. Sing, Reporting physisorption data for gas/solid systems with special reference to the determination of surface area and porosity (Recommendations 1984), Pure and Applied Chemistry, 57 (1985) 603-619.

[37] L. Du, C. Xu, J. Liu, Y. Lan, P. Chen, One-step detonation-assisted synthesis of Fe3O4-Fe@BCNT composite towards high performance lithium-ion batteries, Nanoscale, 9 (2017) 14376-14384.

[38] C.R. Minitha, R.T. Rajendrakumar, Synthesis and characterization of reduced graphene oxide, Advanced Materials Research, 678 (2013) 56-60.

[39] Y. Guo, Z. Zeng, Y. Zhu, Z. Huang, Y. Cui, J. Yang, Catalytic oxidation of aqueous organic contaminants by persulfate activated with sulfur-doped hierarchically porous carbon derived from thiophene, Appl Catal B-Environ, 220 (2018) 635-644.

[40] S. Ye, M. Cheng, G. Zeng, X. Tan, H. Wu, J. Liang, M. Shen, B. Song, J. Liu, H. Yang, Y. Zhang, Insights into catalytic removal and separation of attached metals from natural-aged microplastics by magnetic biochar activating oxidation process, Water Research, 179 (2020) 115876.

[41] Q. Fan, J. Sun, L. Chu, L. Cui, G. Quan, J. Yan, Q. Hussain, M. Iqbal, Effects of chemical oxidation on surface oxygen-containing functional groups and adsorption behavior of biochar, Chemosphere, 207 (2018) 33-40.

[42] P. Xiao, X. Yi, M. Wu, X. Wang, S. Zhu, B. Gao, Y. Liu, H. Zhou, Catalytic performance and periodate activation mechanism of anaerobic sewage sludge-derived biochar, Journal of Hazardous Materials, 424 (2022) 127692.

[43] P. Huang, P. Zhang, C. Wang, J. Tang, H. Sun, Enhancement of persulfate activation by Fe-

biochar composites: Synergism of Fe and N-doped biochar, Appl Catal B-Environ, 303 (2022) 120926.
[44] Z. Xu, Z. Wan, Y. Sun, X. Cao, D. Hou, D.S. Alessi, Y.S. Ok, D.C.W. Tsang, Unraveling iron speciation on Fe-biochar with distinct arsenic removal mechanisms and depth distributions of As and Fe, Chemical Engineering Journal, 425 (2021) 131489.
[45] S. Bakshi, C. Banik, S.J. Rathke, D.A. Laird, Arsenic sorption on zero-valent iron-biochar complexes, Water Research, 137 (2018) 153-163.
[46] Y. Zong, H. Zhang, Y. Shao, W. Ji, Y. Zeng, L. Xu, D. Wu, Surface-mediated periodate activation by nano zero-valent iron for the enhanced abatement of organic contaminants, Journal of Hazardous Materials, 423 (2022) 126991.
[47] S. Wang, J. Wang, Kinetics of PMS activation by graphene oxide and biochar, Chemosphere, 239 (2020) 124812.
[48] S. Xiong, Y. Deng, D. Gong, R. Tang, J. Zheng, L. Li, Z. Zhou, L. Su, C. Liao, L. Yang, Magnetically modified in-situ N-doped Enteromorpha prolifera derived biochar for peroxydisulfate activation: Electron transfer induced singlet oxygen non-radical pathway, Chemosphere, 284 (2021) 131404.
[49] Y. Gu, Y. Xue, D. Zhang, Adsorption of aniline by magnetic biochar with high magnetic separation efficiency, Environmental Pollutants and Bioavailability, 33 (2021) 66-75.
[50] N. Bombuwala Dewage, A.S. Liyanage, Q. Smith, C.U. Pittman, F. Perez, E.B. Hassan, D. Mohan, T. Mlsna, Fast aniline and nitrobenzene remediation from water on magnetized and nonmagnetized Douglas fir biochar, Chemosphere, 225 (2019) 943-953.
[51] X. Liu, Y. Liu, H. Qin, Z. Ye, X. Wei, W. Miao, D. Yang, S. Mao, Selective Removal of Phenolic Compounds by Peroxydisulfate Activation: Inherent Role of Hydrophobicity and Interface ROS, Environmental Science & Technology, 56 (2022) 2665-2676.
[52] P. Rao, E. Hayon, Redox potentials of free radicals. I. Simple organic radicals, Journal of the American Chemical Society, 96 (1974) 1287-1294.
[53] W. He, Y.-T. Zhou, W.G. Wamer, M.D. Boudreau, J.-J. Yin, Mechanisms of the pH dependent generation of hydroxyl radicals and oxygen induced by Ag nanoparticles, Biomaterials, 33 (2012) 7547-7555.
[54] L. He, C. Yang, J. Ding, M.-Y. Lu, C.-X. Chen, G.-Y. Wang, J.-Q. Jiang, L. Ding, G.-S. Liu, N.-Q. Ren, S.-S. Yang, Fe, N-doped carbonaceous catalyst activating periodate for micropollutant removal: Significant role of electron transfer, Appl Catal B-Environ, 303 (2022) 120880.
[55] R. Li, J. Wang, H. Wu, Z. Zhu, H. Guo, Periodate activation for degradation of organic contaminants: Processes, performance and mechanism, Separation and Purification Technology, 292 (2022) 120928.
[56] L. He, Y. Shi, Y. Chen, S. Shen, J. Xue, Y. Ma, L. Zheng, L. Wu, Z. Zhang, L. Yang, Iron-manganese oxide loaded sludge biochar as a novel periodate activator for thiacloprid efficient degradation over a wide pH range, Separation and Purification Technology, 288 (2022) 120703.
[57] Y.-H. Guan, J. Ma, X.-C. Li, J.-Y. Fang, L.-W. Chen, Influence of pH on the Formation of Sulfate and Hydroxyl Radicals in the UV/Peroxymonosulfate System, Environmental Science & Technology, 45 (2011) 9308-9314.
[58] Y. Long, J. Dai, S. Zhao, Y. Su, Z. Wang, Z. Zhang, Atomically Dispersed Cobalt Sites on Graphene as Efficient Periodate Activators for Selective Organic Pollutant Degradation, Environmental

Science & Technology, 55 (2021) 5357-5370.

[59] J. Du, G. Xiao, Y. Xi, X. Zhu, F. Su, S.H. Kim, Periodate activation with manganese oxides for sulfanilamide degradation, Water Research, 169 (2020) 115278.

[60] X. Li, X. Liu, C. Qi, C. Lin, Activation of periodate by granular activated carbon for acid orange 7 decolorization, Journal of the Taiwan Institute of Chemical Engineers, 68 (2016) 211-217.

[61] J. Ma, Degradation of atrazine by manganese-catalysed ozonationâ□”influence of radical scavengers, Water Research, 34 (2000) 3822-3828.

[62] R. Yuan, S.N. Ramjaun, Z. Wang, J. Liu, Effects of chloride ion on degradation of Acid Orange 7 by sulfate radical-based advanced oxidation process: implications for formation of chlorinated aromatic compounds, Journal of Hazardous Materials, 196 (2011) 173-179.

[63] L. Peng, Y. Shang, B. Gao, X. Xu, Co3O4 anchored in N, S heteroatom co-doped porous carbons for degradation of organic contaminant: role of pyridinic N-Co binding and high tolerance of chloride, Appl Catal B-Environ, 282 (2021) 119484.

[64] X. Tian, C. Tian, Y. Nie, C. Dai, C. Yang, N. Tian, Z. Zhou, Y. Li, Y. Wang, Controlled synthesis of dandelion-like NiCo2O4 microspheres and their catalytic performance for peroxymonosulfate activation in humic acid degradation, Chemical Engineering Journal, 331 (2018) 144-151.

[65] M.E. Lindsey, M.A. Tarr, Inhibition of Hydroxyl Radical Reaction with Aromatics by Dissolved Natural Organic Matter, Environmental Science & Technology, 34 (1999) 444-449.

[66] Y. Li, J. Li, Y. Pan, Z. Xiong, G. Yao, R. Xie, B. Lai, Peroxymonosulfate activation on FeCo2S4 modified g-C3N4 (FeCo2S4-CN): Mechanism of singlet oxygen evolution for nonradical efficient degradation of sulfamethoxazole, Chemical Engineering Journal, 384 (2020) 123361.

[67] L. Chen, J. Duan, P. Du, W. Sun, B. Lai, W. Liu, Accurate identification of radicals by in-situ electron paramagnetic resonance in ultraviolet-based homogenous advanced oxidation processes, Water Research, 221 (2022) 118747.

[68] A. Boukir, S. Fellak, P. Doumenq, Structural characterization of Argania spinosa Moroccan wooden artifacts during natural degradation progress using infrared spectroscopy (ATR-FTIR) and X-Ray diffraction (XRD), Heliyon, 5 (2019) e02477.

[69] P. Xiao, X. Yi, M. Wu, X. Wang, S. Zhu, B. Gao, Y. Liu, H. Zhou, Catalytic performance and periodate activation mechanism of anaerobic sewage sludge-derived biochar, Journal of Hazardous Materials, 424 (2022) 127692.

[70] E. Neyens, J. Baeyens, A review of classic Fenton's peroxidation as an advanced oxidation technique, Journal of Hazardous Materials, 98 (2003) 33-50.

[71] X. Zheng, X. Niu, D. Zhang, M. Lv, X. Ye, J. Ma, Z. Lin, M. Fu, Metal-based catalysts for persulfate and peroxymonosulfate activation in heterogeneous ways: A review, Chemical Engineering Journal, 429 (2022) 132323.

[72] Z. Wang, J. Jiang, S. Pang, Y. Zhou, C. Guan, Y. Gao, J. Li, Y. Yang, W. Qiu, C. Jiang, Is Sulfate Radical Really Generated from Peroxydisulfate Activated by Iron(II) for Environmental Decontamination?, Environmental Science & Technology, 52 (2018) 11276-11284.

[73] Q. Wang, H. Zeng, Y. Liang, Y. Cao, Y. Xiao, J. Ma, Degradation of bisphenol AF in water by periodate activation with FeS (mackinawite) and the role of sulfur species in the generation of sulfate radicals, Chemical Engineering Journal, 407 (2021) 126738.

[74] T. Yang, D. Yu, D. Wang, T. Yang, Z. Li, M. Wu, M. Petru, J. Crittenden, Accelerating

Fe(Ⅲ)/Fe(Ⅱ) cycle via Fe(Ⅱ) substitution for enhancing Fenton-like performance of Fe-MOFs, Appl Catal B-Environ, 286 (2021) 119859.

[75] J. Moan, On the diffusion length of singlet oxygen in cells and tissues, Journal of Photochemistry and Photobiology B: Biology, 6 (1990) 343-344.

[76] J.M.P. Martirez, E.A. Carter, Unraveling Oxygen Evolution on Iron-Doped beta-Nickel Oxyhydroxide: The Key Role of Highly Active Molecular-like Sites, Journal Of The American Chemical Society, 141 (2019) 693-705.

[77] J. Dec, J.-M. Bollag, Effect of various factors on dehalogenation of chlorinated phenols and anilines during oxidative coupling, Environmental Science & Technology, 29 (1995) 657-663.

[78] B. Ou, J. Wang, Y. Wu, S. Zhao, Z. Wang, A highly efficient cathode based on modified graphite felt for aniline degradation by electro-Fenton, Chemosphere, 235 (2019) 49-57.

[79] X. Zheng, T. Xu, X. Kang, Y. Xing, Y. Cao, X. Gui, Structural dependent persulfate activation by coke powder for aniline degradation, Chemical Engineering Journal, 431 (2022) 134088.

[80] J. Zhu, C. Chen, Y. Li, L. Zhou, Y. Lan, Rapid degradation of aniline by peroxydisulfate activated with copper-nickel binary oxysulfide, Separation and Purification Technology, 209 (2019) 1007-1015.

[81] C. Bai, Y. Liu, C. Wang, X.-C. Zhang, J.-X. Wu, H.-T. Ren, X. Han, Conversion of aniline contaminant to valuable polyaniline polymers from wastewater under alkaline conditions, Molecular Catalysis, 503 (2021) 111430.

[82] H. Shang, Y. Xia, Y. Zhou, G. Liu, X. Hu, Removal of aniline from wastewater by electro-polymerization with superior energy efficiency, Environmental Research, 190 (2020) 109931.

[83] P. Ding, H. Ji, P. Li, Q. Liu, Y. Wu, M. Guo, Z. Zhou, S. Gao, W. Xu, W. Liu, Q. Wang, S. Chen, Visible-light degradation of antibiotics catalyzed by titania/zirconia/graphitic carbon nitride ternary nanocomposites: a combined experimental and theoretical study, Appl Catal B-Environ, 300 (2022) 120633.